Supplementary Information:

3D-printed fluidic networks for high-power-density heat-managing miniaturized redox flow batteries

Julian Marschewski[a,b], Lorenz Brenner[a], Neil Ebejer[b], Patrick Ruch[b], Bruno Michel[b], Dimos Poulikakos[a,*]

[a]Laboratory of Thermodynamics in Emerging Technologies, Department of Mechanical and Process Engineering, ETH Zürich, 8092 Zürich, Switzerland

[b]IBM Research Zurich, Säumerstrasse 4, 8803 Rüschlikon, Zürich, Switzerland

[*]Corresponding author. E-mail address: dpoulikakos@ethz.ch

Supplementary Note 1 : Flow uniformity (µPIV measurements)

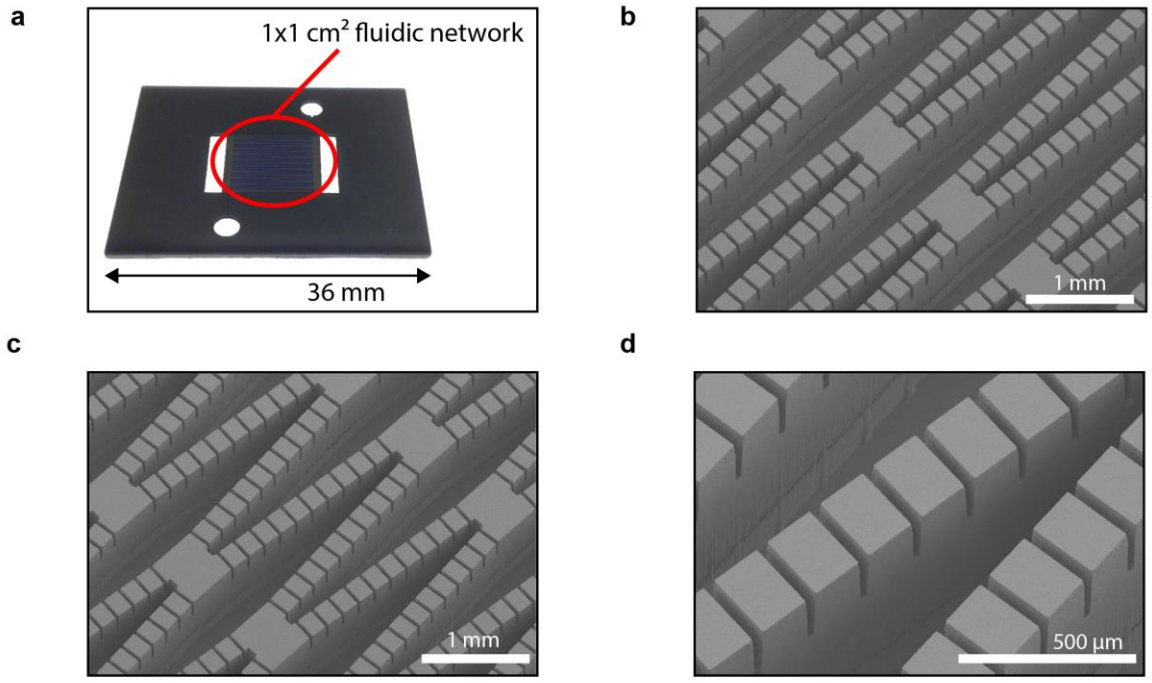

Supplementary Figure 1: Photograph and scanning electron micrographs of the silicon micromachined test devices to study the flow uniformity in the fluidic networks. The flow resistance due to the pressure drop through the porous electrode is mimicked with rows of slits. (a) Overview of the Si test device. After etching the silicon device is closed with a glass cover by wafer-scale anodic bonding. (b) Interdigitated channels, tapered and dual-pass. (c) Interdigitated channels, tapered and quadruple-pass. (d) Zoomed view of the etched slits.

Flow field measurements were performed using micro particle image velocimetry (µPIV). We employed a system from LaVision GmbH in our laboratory[1] and 1 µm particles (Invitrogen nile red FluoSpheres). Silicon-based test chips (see Supplementary Fig. 1) were fabricated using a series of microelectromechanical systems standard fabrication processes as in earlier work[1], starting from 100 mm, <100>-oriented, single-side polished 1000 µm thick

silicon wafers. The cavity was closed by wafer-level anodic bonding of a borofloat glass wafer to the processed Si wafer.

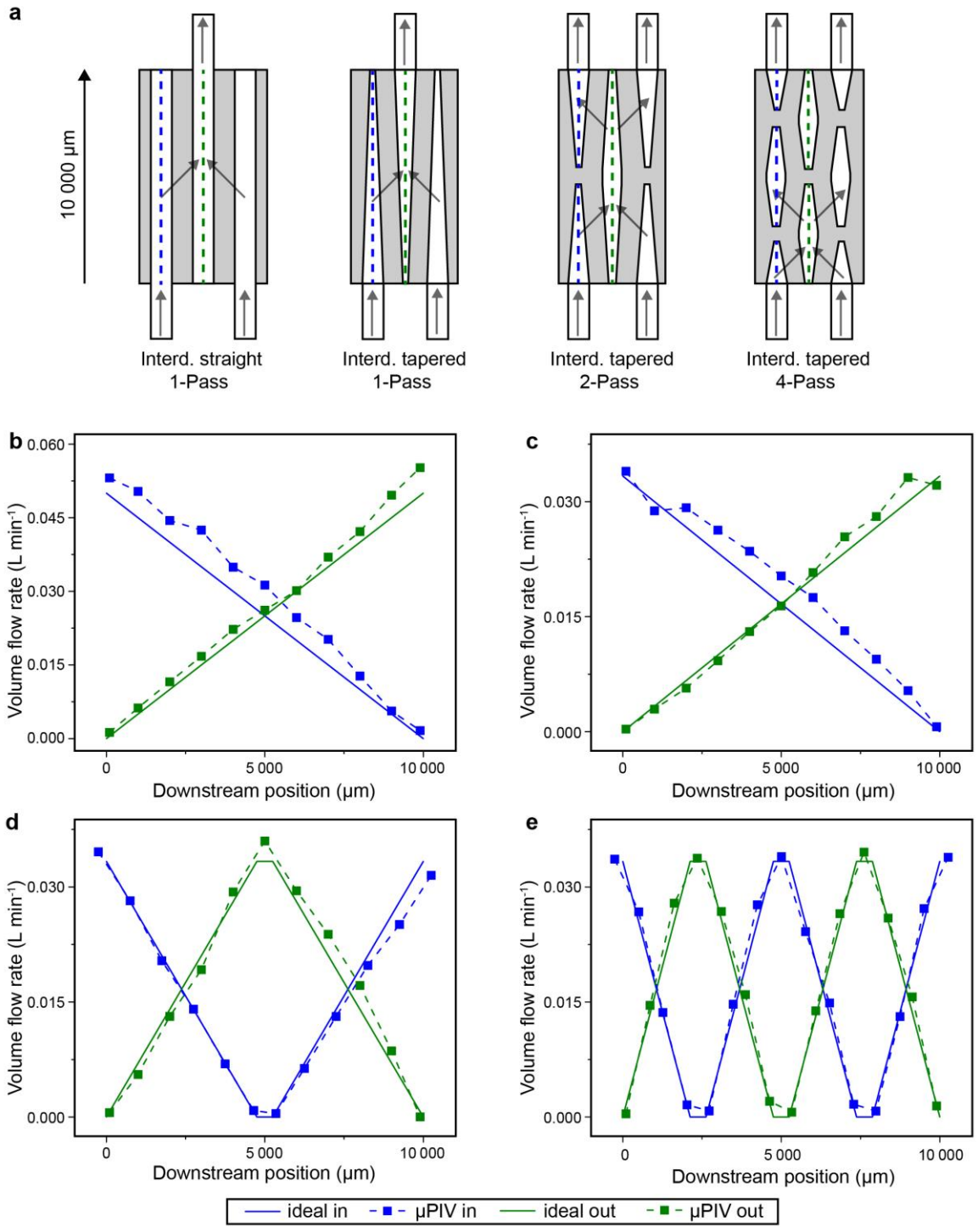

Supplementary Figure 2: Flow uniformity in interdigitated fluidic networks at a total flow rate of 0.3 L/min studied using µPIV. The flow profiles in two adjacent in- and outlet channels are measured in order to investigate how the fluid is

guided in the interdigitated network. (a) Illustration of fluidic networks. Blue dashed lines indicate the inlet channels, green dashed lines the outlet channel. (b) Interdigitated channels, straight and single-pass. (c) Interdigitated channels, tapered and single-pass. (d) Interdigitated channels, tapered and dual-pass. (e) Interdigitated channels, tapered and quadruple-pass.

The interdigitation of inlet and outlet channels results in an increase in mass transfer. We investigate the flow distribution within the fluidic network with µPIV measurements in micro-machined silicon devices. In these experiments etched slits mimic the porous electrode and bring about the necessary pressure drop between two adjacent channels. The channels of the basic interdigitated design were dimensioned according to the framework developed by Kee and Zhu[2]. Supplementary Fig. 2b-e show the experimental data obtained in the center channels of the fluidic networks after confirming that the header is sufficiently large to yield even distribution among the individual channels[3]. In the ideal case, the volume flow rate decreases linearly in the inlet ('feed') channels and vice versa increases linearly in the outlet ("exhaust") channels (see Supplementary Fig. 2a). In this situation the flow is uniformly distributed and transverses evenly across the walls between two adjacent channels.

Supplementary Fig. 2b,c show the single-pass configuration with both straight and tapered channels. Already in the basic interdigitated configuration with straight channels (Supplementary Fig. 2b) the experimentally observed distribution is close to ideal (solid lines) due to the dimensioning process[2]. The introduction of tapering results in decreased volume flow rates in the channels due to the higher number of inlet channels among which the overall volume flow rate of 0.3 L/min is distributed. The successive introduction of multiple-pass structures enhances the flow uniformity further and the measured data in the in- and outlet channels seem closely mirrored as shown in Supplementary Fig. 2d,e.

Supplementary Note 2: Diffusion resistance

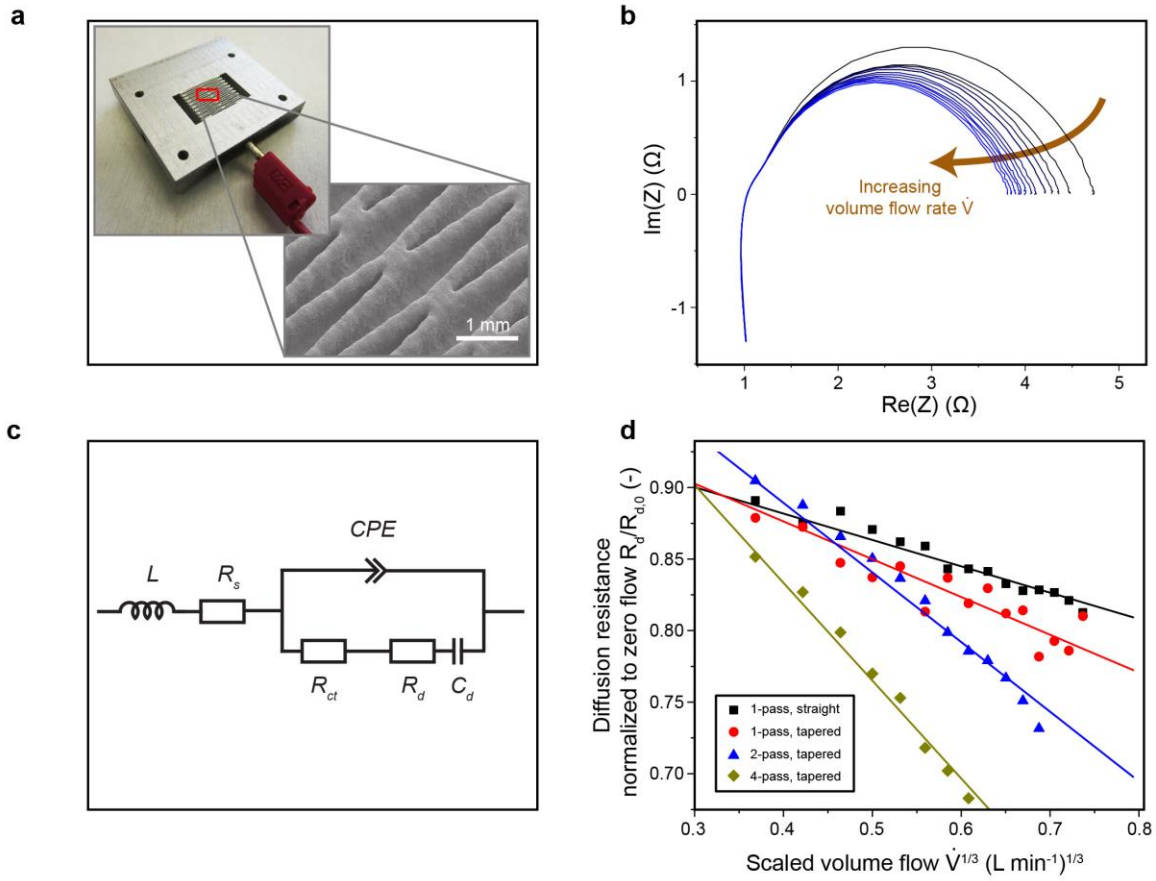

Supplementary Figure 3: Diffusion resistance measurements. (a) Photograph of 3D-printed experimental device, sputtered with 300 nm Pt. The enlargement shows a scanning electron micrograph of the channel structures. (b) Electrochemical impedance spectrograms in 5 mM potassium ferro-/ferricyanide and 0.5 M potassium sulfate as a function of flow rate (fluidic network: tapered dual-pass). (c) Equivalent electrical circuit used to model to electrochemical impedance spectroscopy measurements (*L*: inductance, R_s: series resistance, *CPE*: constant phase element, R_{ct}: charge transfer resistance, R_d: diffusion resistance, and C_d: diffusion capacitance). (d) Normalized diffusion resistance comparing the four tested fluidic networks. On the x-axis the volume flow rate is scaled to the power of 1/3.

By using electrochemical impedance spectroscopy in equimolar solutions of both 5 mM potassium ferrocyanide and 5 mM potassium ferricyanide in 0.5 M K_2SO_4 we probed the diffusion resistance. Test devices were made by 3D-printing (see Supplementary Fig. 3a) and subsequently sputtered with 300 nm Pt. As a separator Celgard 3501 (kindly supplied by Celgard, LLC, USA) was used to separate two porous carbon paper electrodes (Spectracarb 2050 A). Supplementary Fig. 3b shows typical Nyquist plots obtained at varying flow rates for the tapered dual-pass fluidic network (frequency range: 200 kHz – 100 mHz with 9 measurements per decade, applied voltage: 0.3 V, amplitude: 10 mV, averaged over 3 measurements per frequency). With increasing flow rates the right limit of the large semicircle moves inward, which indicates that the diffusion resistance decreases. On the other hand, the ohmic resistance, defined as the left intercept with the $Im(Z) = 0$ line, is independent of flow rate.

In Supplementary Fig. 3c we draw an equivalent electrical circuit (where *L*: inductance, R_s: series resistance, *CPE*: constant phase element, R_{ct}: charge transfer resistance, R_d: diffusion resistance, and C_d: diffusion capacitance), in which the diffusion resistance appears in parallel to a constant phase element. This diffusion resistance we derive from the Nyquist plots by a fitting procedure.

Supplementary Fig. 3d summarizes our findings on this diffusion resistance for the four different channel networks tested. In order to allow a comparison we normalized the measured diffusion resistance at flow, R_d, with respect to the diffusion resistance at no flow, $R_{d,0}$. On the x-axis we scaled the volume flow rate to the power of 1/3, i.e. $\dot{V}^{1/3}$. We observe good agreement with a linear fit of our data, which indicates that the laminar flow assumption holds true. Furthermore, the diffusion resistance is clearly a function of the fluidic network design as the slope of the linear fits in Supplementary Fig. 3d change with the different design iterations. The interdigitated device with straight channels shows the flattest slope, while the device with four passes has the steepest slope. This observation can be explained with the more homogeneous flow distribution of the multiple-pass devices, but also with the

increase of the superficial velocity of the electrolyte through the porous electrode.

Supplementary Figures

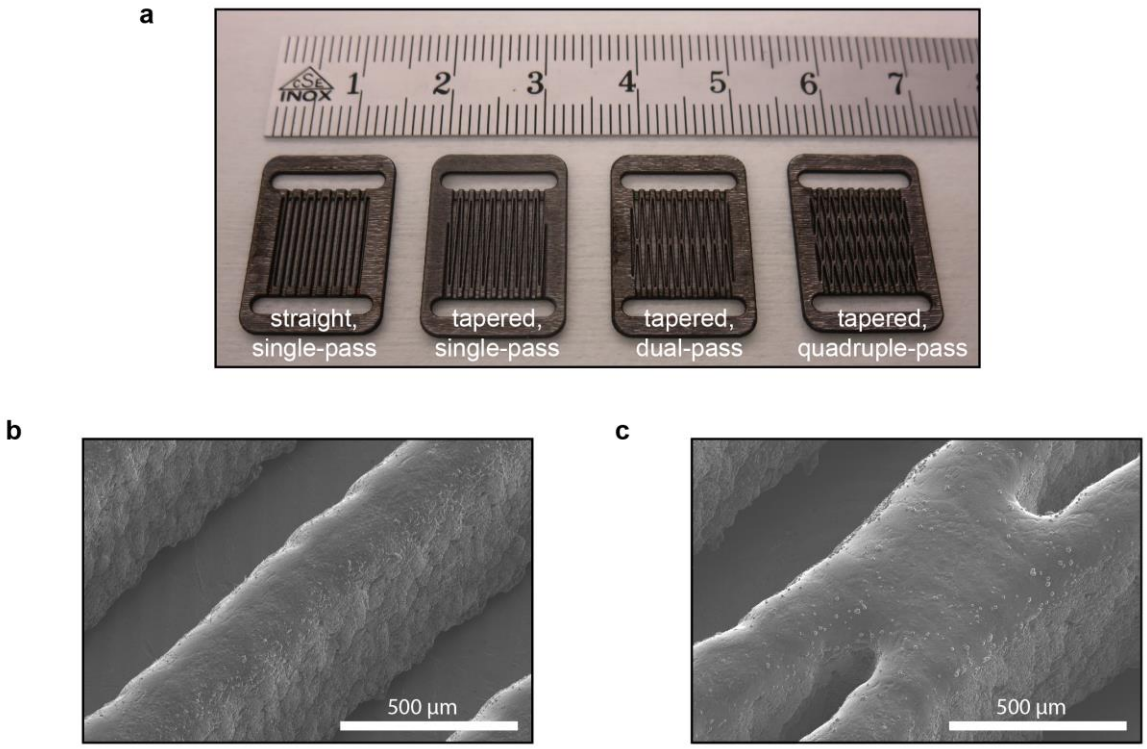

Supplementary Figure 4: Photographs and scanning electron micrographs of the 3D-printed fluidic networks after metallization and passivation. (a) Fluidic networks with interdigitated microchannels developed in this work. The scale of the ruler is in cm. (b) Surface quality of the 3D-printed structures. (c) A flow-blocking element in the design with four passes.

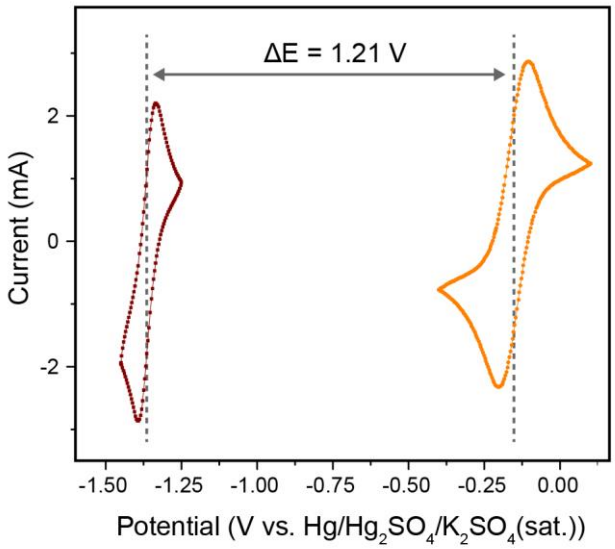

Supplementary Figure 5: Cyclic voltammetry of electrolytes. 0.2 M 2,6-DHAQ in 2 M KOH (wine-colored curve) and 0.4 M potassium ferrocyanide in 1 M KOH (orange-colored curve), scanned at 25 mV/s on glassy carbon electrode. Counter electrode: Pt, reference electrode: $Hg/Hg_2SO_4/K_2SO_4$(sat.).

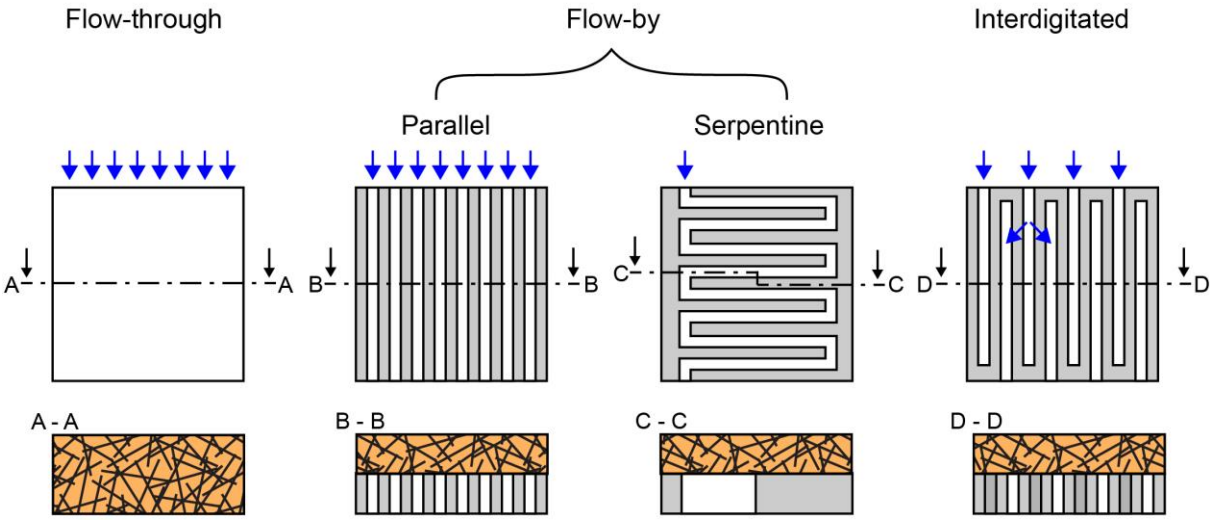

Supplementary Figure 6: Illustration of common flow guidance concepts in RFBs. From left to right: flow-through, flow-by (parallel and serpentine channels), and interdigitated channels. At top the top view is given, below a cut at the indicated positions. The channels are in white, the ribs in gray, and the porous electrode patterned with an orange background. Blue arrows indicate the electrolyte inflow.

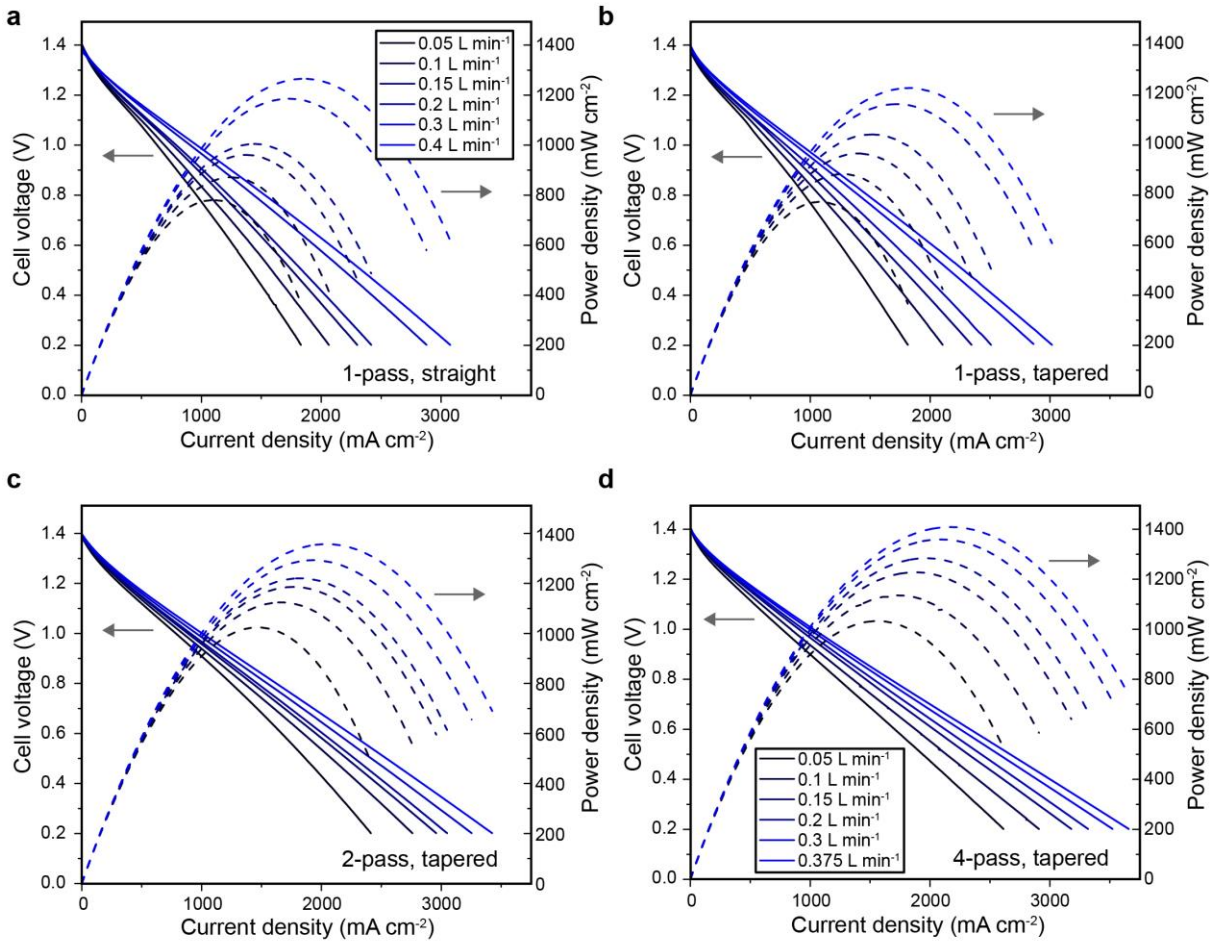

Supplementary Figure 7: Polarization curves and power density in concentrated solutions of 0.2 M 2,6-DHAQ and 0.4 M ferrocyanide. (a) Straight channels, single pass, (b) tapered channels, single-pass, (c) tapered channels, dual-pass, and (d) tapered channels, quadruple-pass. The legend in (b) and (c) is the same as in (a).

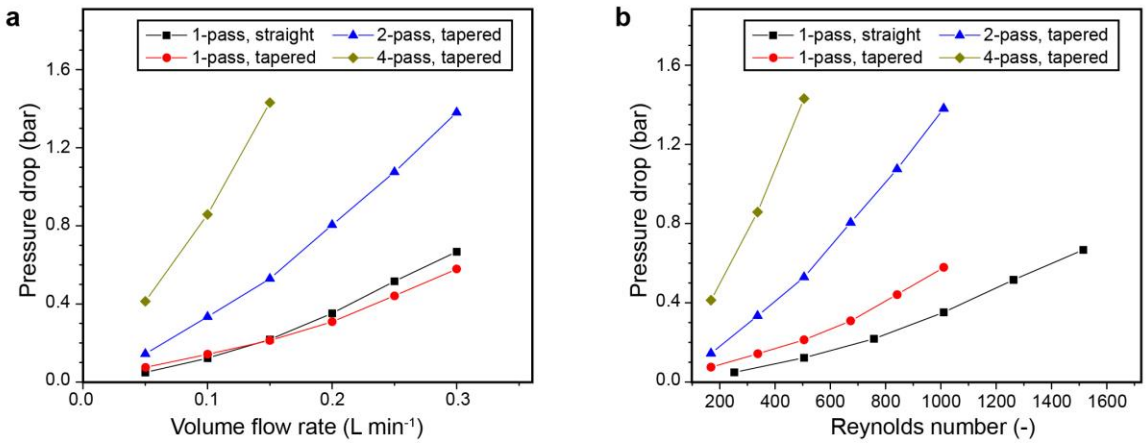

Supplementary Figure 8: Pressure drop per half-cell. (a) Volume flow rate versus pressure drop and (b) Reynolds number versus pressure drop.

The pressure drops are measured with water as the working fluid in the range from 0.05 $Lmin^{-1}$ to 0.3 $Lmin^{-1}$, see Supplementary Fig. 8a. In Supplementary Fig. 8b the pressure drops are shown as a function of Reynolds number, calculated with the kinematic viscosity of water. As the characteristic length the hydraulic diameter of the rectangular microchannel with dimensions of 500 µm x 600 µm at the very entrance is used. The single-pass design of the fluidic networks with straight channels features in total 6 inlet channels, whereas all other designs feature 9 inlet channels. This difference in the overall inlet channel count explains why the Reynolds numbers for the same flow rates are larger in the single-pass design with straight channels.

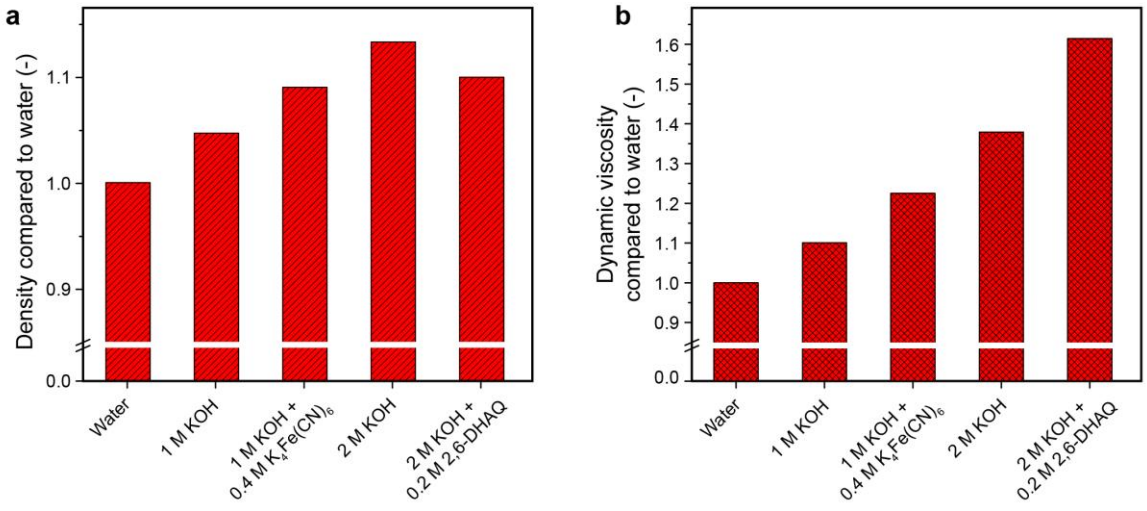

Supplementary Figure 9: Electrolyte properties at room temperature in comparison to water. (a) Density and (b) dynamic viscosity.

Both the densities and dynamic viscosities of the 1 M and 2 M KOH solutions compare very well to literature values[4].

Supplementary References

1. J. Marschewski, S. Jung, P. Ruch, N. Prasad, S. Mazzotti, B. Michel, and D. Poulikakos, *Lab Chip*, 2015, **15**, 1923–1933.
2. R. J. Kee and H. Zhu, *J. Power Sources*, 2015, **299**, 509–518.
3. W. Wagner, *Strömung und Druckverlust*, Vogel Business Media, Würzburg, 7th edn., 2012.
4. P. M. Sipos, G. Hefter, and P. M. May, *J. Chem. Eng. Data*, 2000, **45**, 613–617.